Z. Phys. C – Particle and Fields 27, 329–339 (1985)

Zeitschrift für Physik C Particles and Fields

Inclusive Particle Production in the Transverse Momentum Range Between 0.25 and 40 GeV/c at the CERN $Sp\bar{p}S$ Collider

UA2 Collaboration

M. Banner[6], Ph. Bloch[6,a], F. Bonaudi[2], K. Borer[1], M. Borghini[2], J.C. Chollet[4], A.G. Clark[2], C. Conta[5], P. Darriulat[2], L. Di Lella[2], J. Dines Hansen[3], P.A. Dorsaz[2,b], L. Fayard[4], M. Fraternali[5], D. Froidevaux[4], J.M. Gaillard[4], O. Gildemeister[2], V.G. Goggi[5], B. Hahn[1], H. Hänni[1], J.R. Hansen[2], P. Hansen[2,3], T. Himel[2,c], V. Hungerbühler[2,d], P. Jenni[2], O. Kofoed-Hansen[3], E. Lançon[6], M. Livan[2,5], S. Loucatos[6], B. Madsen[3], P. Mani[1], B. Mansoulié[6], G.C. Mantovani[e], L. Mapelli[2,f], B. Merkel[4], R. Møllerud[3], C. Onions[2], G. Parrour[4], F. Pastore[5], H. Plothow-Besch[2,4], M. Polverel[6], J.P. Repellin[4], A. Rimoldi[5], A. Rothenberg[2,c], A. Roussarie[6], G. Sauvage[4], J. Schacher[1], J.L. Siegrist[2,g], F. Stocker[1], J. Teiger[6], V. Vercesi[5], A. Weidberg[2], H. Zaccone[6], W. Zeller[1,h]

[1] Laboratorium für Hochenergiephysik, Universität Bern, Sidlerstrasse 5, CH-3012 Bern, Switzerland
[2] CERN, CH-1211 Geneva 23, Switzerland
[3] Niels Bohr Institute, Blegdamsvej 17, DK-2100 Copenhagen, Denmark
[4] Laboratoire de l'Accélérateur Linéaire, Université de Paris-Sud, F-91405 Orsay, France
[5] Dipartimento di Fisica Nucleare e Teorica, Università di Pavia and INFN, Sezione di Pavia, Via Bassi 6, I-27100 Pavia, Italy
[6] Centre d'Etudes Nucléaires de Saclay, F-91191 Gif sur Yvette, France

Abstract. Inclusive particle production cross-sections have been measured at the $Sp\bar{p}S$ collider using the UA2 detector in various ranges of transverse momentum (P_T) and pseudo-rapidity (η). Cross-section measurements are presented for π^0 production ($P_T \leqq 15$ GeV/c, $|\eta| \leqq 0.85$ and $P_T \leqq 40$ GeV/c, $1.0 \leqq |\eta| \leqq 1.8$), for η meson production ($3 \leqq P_T \leqq 6$ GeV/c, $|\eta| \leqq 0.85$) and for charged particle production ($P_T \leqq 10$ GeV/c, $1.0 \leqq |\eta| \leqq 1.8$). Results are compared with the predictions of QCD calculations.

1. Introduction

The UA2 detector, installed at the $Sp\bar{p}S$ collider, is used to measure inclusive particle production in two different regions of pseudorapidity η. In these regions it is equipped with magnetic spectrometers and with highly segmented electromagnetic calorimeters, giving accurate momentum and energy measurements and the necessary resolving power between nearby particles.

The first of these regions covers the full azimuthal range and the forward (F) and backward (B) pseudorapidity intervals $1.0 \leqq |\eta| \leqq 1.8$.

The second of these regions covers a 28° azimuthal wedge in the central region, $|\eta| \leqq 0.63$, and was used during the 1981 and 1982 data taking periods of the $p\bar{p}$ collider. It was later replaced by calorimeters, providing a geometry better suited to the search for the electroweak bosons. Measurements performed in 1981 in this region have been previously published [1, 2].

In the present paper we present measurements of charged particle and π^0 production cross-sections performed in the F/B region, together with an analysis of the π^0 and η meson data collected in 1982 in the wedge region.

[a] Now at CERN, Switzerland
[b] Now at University of Geneva, Switzerland
[c] Now at SLAC, Stanford University, Stanford, USA
[d] Now at Lecroy Research Systems, Geneva, Switzerland
[e] Gruppo INFN del Dipartimento di Fisica dell' Università di Perugia, Italy
[f] On leave from INFN, Pavia, Italy
[g] Now at Dept. of Physics, University of California, Berkeley, USA
[h] Now at Abteilung für Strahlenschutz, Eidgenössisches Gesundheitsamt, BERN, Switzerland

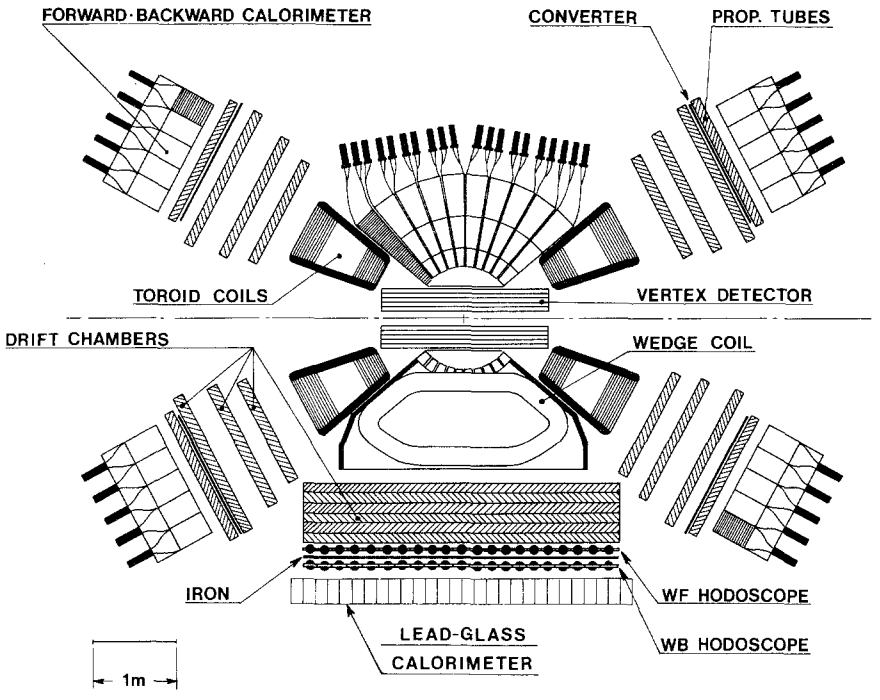

Fig. 1. The UA2 detector: schematic cross-section in the horizontal plane containing the beam

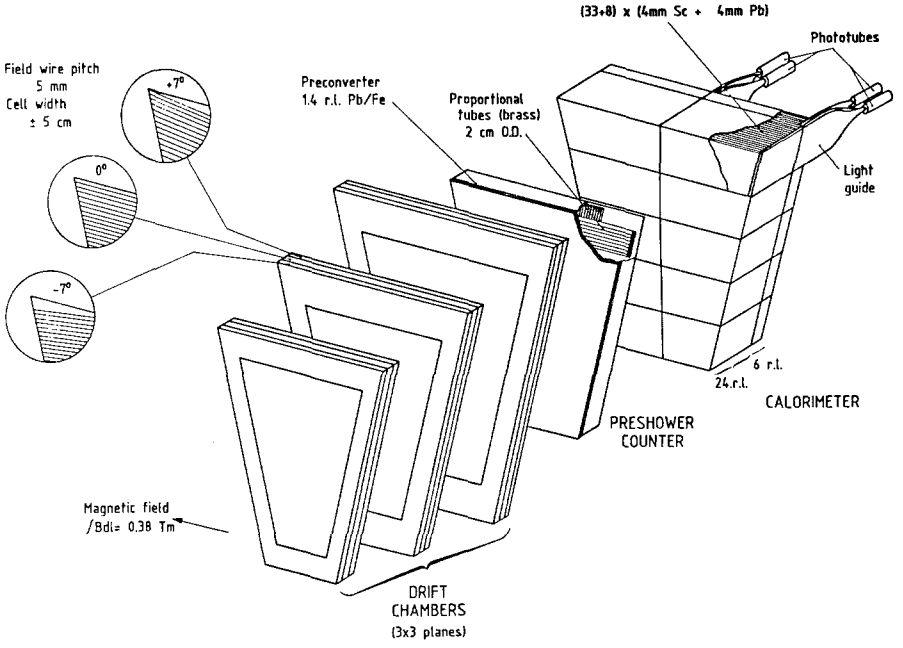

Fig. 2. Schematic view of one of the 24 sectors of the F/B detectors

2. Experimental Set-up

The UA2 detector, shown schematically in Fig. 1, has been described in detail in earlier publications [1 to 7]. In the present section we recall the main characteristics of the two parts of the detector which are of relevance to the present study: the F/B and wedge spectrometers (Figs. 2 and 3). Both spectrometers share a common tracking device surrounding the interaction region, the vertex detector. They consist otherwise of separate detectors, including in sequence a magnetic field region, a set of drift chambers, a preshower counter and an electromagnetic calorimeter.

The vertex detector [4] consists of cyclindrical proportional and drift chambers. The localization of the interaction point is obtained with a precision of ± 1 mm in all directions.

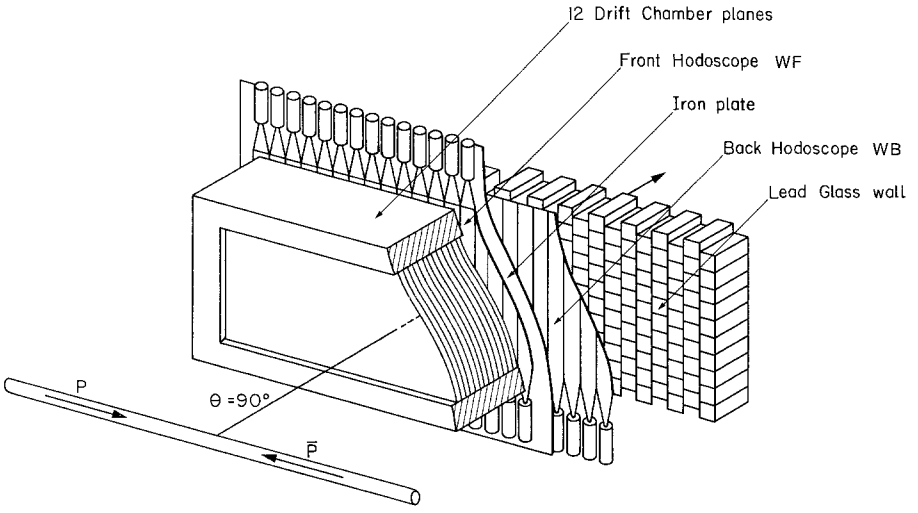

Fig. 3. Exploded view of the wedge detector. Front elements have been partly cut in order to make those in the back visible

In each of the F/B regions ($20° < \theta < 37.5°$ and $142.5° < \theta < 160°$) a toroidal magnetic field, with an average field integral of 0.38 Tm, is provided by twelve magnet coils. Each sector covers 30° in azimuth, of which 20% are obscured by the magnet coils, and is instrumented with:

a) Three drift chambers located behing the magnetic field region. Each chamber consists of three planes, with wires at $-7°$, 0° and $+7°$ with respect to the field direction [5].

b) A 1.4 radiation length thick lead-iron converter, followed by a preshower detector made of 20 mm diameter proportional tubes (MTPC) [6]. This detector consists of two planes, each with two layers of tubes staggered by a tube radius. The tube direction is parallel to the magnetic field for the first set, and at 77° to it for the second set. The pulse heights of the tube signals are recorded.

c) An electromagnetic calorimeter (the F/B calorimeter) divided into ten independent cells, each covering 15° in φ and 3.5° in θ. Each cell is segmented in depth into two independent compartments, 24 and 6 radiation lengths thick respectively, the latter providing rejection against hadrons. Each compartment is made of a multi-layer sandwich of lead and scintillator plates (each plate is 4 mm thick), and is read out by two BBQ-doped light guides on opposite sides of the cell. Only the first compartment is used for the electromagnetic energy measurement. The resolution is measured in a 40 GeV electron beam to be $0.17/\sqrt{E}$, dominated by sampling fluctuations.

In the wedge region ($56° < \theta < 124°$, $-14° < \varphi < +14°$) the spectrometer, shown in Fig. 3, consists of:

a) A dipole magnet, followed by a set of twelve drift chamber planes used for charged particle momentum measurement.

b) Two counter hodoscopes (*WF* and *WB*) separated by a 2 cm thick iron plate used as a converter. The front hodoscope scintillators (*WF*), equipped with phototubes at both ends, measure time of flight and ionization. The *WB* hodoscope scintillators, equipped with phototubes at one end only, measure ionization.

c) An array of 280 lead-glass blocks, 15×15 cm^2 each in cross-section, 14.5 radiation lengths thick. The energy resolution for photons and electrons is measured to be:

$$\frac{\Delta E}{E} = \sqrt{(3.4)^2 + \frac{(5.7)^2}{E}} \text{ in } \%, \quad (E \text{ in GeV}).$$

All calorimeter cells (forward-backward, wedge lead-glass) were calibrated in 10 GeV electron and muon beams at the CERN *PS*.

The monitoring of short-term fluctuations is made by a system of Xe flashers (one per sector of the F/B calorimeters, and one for each 20 lead-glass cells in the wedge), which generate light pulses that are transmitted by optical fibers to the different light-guides and scintillators of the F/B calorimeters, or to the lead-glass blocks in the wedge [7]. The overall electronic gain of each channel is monitored by calibrated pulses.

In the F/B calorimeters, the long-term monitoring of the calibration is maintained by measuring the direct current induced by the same Co^{60} source positioned in front of each calorimeter cell in its center. These measurements are performed before and after each collider running period.

The systematic uncertainty in the energy calibration of the electromagnetic calorimeters for the data discussed here amounts to an average of $\pm 1.5\%$. The comparison of the different Co^{60} source

measurements over a period of four years shows a cell calibration uncertainty of less than 2% in the F/B calorimeters.

The overall calibration constant for the wedge lead-glass is obtained by measuring the mass of π^0's reconstructed from resolved photon pairs. It differs from an initial calibration with test beam measurements by a factor of 1.045 ± 0.020.

Two scintillator hodoscopes (minimum bias counters) [8], cover the polar angle interval from 0.42° to 5.7° with respect to the beam on both sides of the collision region. They give a coincidence signal (minimum bias signal) in more than 98% of all non-diffractive $p\bar{p}$ collisions. All triggers used in the present analysis require a coincidence with this signal. These counters are also used for the absolute normalization of the measured cross-sections. For this purpose a special trigger (minimum bias trigger) requiring only the minimum bias signal is used simultaneously with all other triggers. The cross-section (σ_{meas}) corresponding to a number of events N_{meas}, is then given by:

$$\sigma_{\text{meas}} = \sigma_{\text{mb}}(N_{\text{meas}}/N_{\text{mb}}),$$

where N_{mb} is the number of minimum bias trigger events recorded during the same period, and σ_{mb} is the cross-section seen by the minimum bias counters, 43.9 ± 3.5 mb as measured by UA4 [8].

Run-to-run fluctuations in the number of recorded minimum bias events, combined with an 8% uncertainty on the inelastic cross-section, result in a 13% overall uncertainty on measured cross-sections.

3. Charged Particle Production

3.1 Data Reduction and Corrections

Charged particle production is analyzed in the F/B spectrometers, at an average pseudorapidity $|\eta| = 1.4$.

The data sample was recorded during the 1982 $\bar{p}p$ period and corresponds to an integrated luminosity of $0.67\ \mu b^{-1}$.

The momentum of the charged particles is computed from measuring their deflection by the toroidal magnets. This deflection is obtained from the position of the interaction point measured by the vertex detector and the direction of the outgoing particle after the magnetic field, determined by the drift chamber system. The precise absolute and relative positions of the wires in the chamber are derived using data taken without magnetic field. A point resolution on a track of $\pm 200\ \mu$ and an angular resolution in the bending plane of ± 0.47 mrad. is achieved. These uncertainties, combined with the 1 mm precision on the interaction point as given by the vertex detector, result in a momentum resolution

$$dP/P = \sqrt{(1.8\,P)^2 + (2.5)^2}\,\% \quad (P \text{ in GeV/c})$$

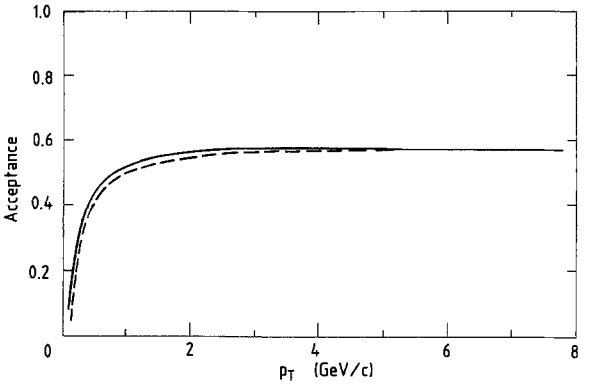

Fig. 4. Acceptance in one hemisphere of the F/B spectrometers for positive (solid line) and negative (dashed line) particles produced at the center of the interaction region

The analysis is limited to transverse momenta in excess of 0.25 GeV/c and to the pseudo-rapidity interval $1 \leqq |\eta| \leqq 1.8$, where the acceptance exceeds 50% of its maximum value. The acceptance in the F/B spectrometers is evaluated using a Monte Carlo simulation assuming the same pion, kaon and proton fractions, as a function of P_T, as measured at $\langle \eta \rangle = 0$ [1]. The particles are generated with uniform distribution in both rapidity and azimuth. The propagation through the detector takes into account the measured magnetic field map, energy losses, multiple scattering and particle decays. The dependence of the acceptance on transverse momentum is shown in Fig. 4 for positive and negative particles produced in the center of the interaction region. This acceptance becomes constant above 1.5 GeV/c at a value of about 0.57 and it drops typically to 0.47 for longitudinal displacements of the vertex of ± 18 cm, which corresponds to 2 standard deviations of the source width distribution for the present data sample.

The Monte Carlo events are reconstructed using the same program as for the real data. Acceptance corrections are applied to all tracks of the data sample according to their charge, transverse momentum, pseudo-rapidity and longitudinal vertex position. A cut on the χ^2 probability $P(\chi^2)$ of the momentum fit selects charged tracks with $P(\chi^2) > 3 \cdot 10^{-3}$.

Overall corrections are applied to the data sample for losses due to vertex and track reconstruction inefficiencies ($\simeq 6\%$) and nuclear interactions ($\simeq 8\%$). In addition the data are corrected for the following P_T dependent effects:

a) Background contamination from spurious tracks. This is estimated by extrapolating the tail of the χ^2 distribution in the momentum fit and varies from 4% at $P_T=0.25$ GeV/c to 20% at $P_T=5$ GeV/c.

b) Particles decaying in flight. This effect is studied using a Monte-Carlo generated sample of $K\to\mu\nu$ decays in the acceptance range, 40% of which have a good momentum fit. The relationship between true N_i^{tr} and observed N_i^{obs} populations in the i-th P_T bin is given by:

$$N_i^{tr}=\frac{N_i^{obs}-\Sigma_j N_j^{obs} f_j^k p_j^r M_{ij}}{1-f_i^k[p_i^l+p_i^r]}$$

where in each bin f^k is the original kaon fraction and p^r, p^l are the probabilities associated to a kaon decay reconstructed or lost in the reconstruction chain, respectively. M_{ij} is a unitary matrix decribing the mixing among different channels associated with the reconstructed kaon decays.

This correction is applied to the distribution of real data after unfolding the experimental distribution. The correction factor varies from 1.0 at $P_T=2$ GeV/c to 1.08 at $P_T=8$ GeV/c.

c) Momentum resolution. A correction to the invariant cross section is applied by parametrizing the P_T dependence of the data as $A/(P_{T0}+P_T)^n$ and using the measured gaussian resolution of $1/P$. This correction is negligible up to transverse momenta of 2 GeV/c and increases with P_T (e.g. 40% at 5 GeV/c). A point-to-point systematic error, arising from the uncertainty on the value of the momentum resolution, is combined in quadrature with the statistical error. It is computed by a variation of $\sigma(1/P)$ of 5% which corresponds to a variation of one unit in the final value of χ^2/d.f. in the overall fit to the data. The increase of the measured errors is less than 10% for momenta of less than 2 GeV/c, and is about 30% at 5 GeV/c.

3.2 Cross Section

The consistency of the results in the forward and backward regions is clearly reflected in the data:

a) The ratio of the cross section in the forward and in the backward regions is independent of P_T and equal to unity:

$$\sigma_F/\sigma_B=1.00\pm0.01$$

b) Given the relative orientations of the magnetic fields, the cross-section ratios between the two hemispheres for hadrons of opposite charges (h^+ and h^-) are expected to be independent of P_T and equal to unity. We find

$$\sigma_F(h^+)/\sigma_B(h^-)=1.01\pm0.02$$

$$\sigma_F(h^-)/\sigma_B(h^+)=0.98\pm0.02$$

Table 1. Inclusive charged particle cross-section at $\langle|\eta|\rangle=1.4$. ($p\bar{p}\to h+$ anything at $\sqrt{s}=540$ GeV)

P_T (GeV/c)	$Ed^3\sigma/dP^3$ (cm^2 GeV^{-2}c^3)	P_T (GeV/c)	$Ed^3\sigma/dP^3$ (cm^2 GeV^{-2}c^3)
0.29	$(8.56\pm0.13)\ 10^{-26}$	2.0	$(8.70\pm0.80)\ 10^{-29}$
0.39	$(4.52\pm0.07)\ 10^{-26}$	2.14	$(5.50\pm0.47)\ 10^{-29}$
0.49	$(2.42\pm0.04)\ 10^{-26}$	2.34	$(3.11\pm0.32)\ 10^{-29}$
0.59	$(1.38\pm0.03)\ 10^{-26}$	2.54	$(2.00\pm0.24)\ 10^{-29}$
0.69	$(8.49\pm0.18)\ 10^{-27}$	2.74	$(1.33\pm0.20)\ 10^{-29}$
0.8	$(5.24\pm0.13)\ 10^{-27}$	2.94	$(7.10\pm1.41)\ 10^{-30}$
0.9	$(3.46\pm0.09)\ 10^{-27}$	3.23	$(6.65\pm0.87)\ 10^{-30}$
1.0	$(2.12\pm0.07)\ 10^{-27}$	3.63	$(3.06\pm0.51)\ 10^{-30}$
1.1	$(1.47\pm0.05)\ 10^{-27}$	4.03	$(1.24\pm0.27)\ 10^{-30}$
1.2	$(1.03\pm0.04)\ 10^{-27}$	4.44	$(7.3\ \pm2.0)\ 10^{-31}$
1.3	$(6.85\pm0.33)\ 10^{-28}$	4.84	$(5.1\ \pm1.5)\ 10^{-31}$
1.4	$(5.08\pm0.28)\ 10^{-28}$	5.24	$(3.3\ \pm1.0)\ 10^{-31}$
1.5	$(3.36\pm0.22)\ 10^{-28}$	5.64	$(2.0\ \pm0.8)\ 10^{-31}$
1.6	$(2.60\pm0.17)\ 10^{-28}$	6.21	$(8.0\ \pm3.0)\ 10^{-32}$
1.7	$(1.86\pm0.14)\ 10^{-28}$	7.01	$(2.8\ \pm1.5)\ 10^{-32}$
1.8	$(1.31\pm0.12)\ 10^{-28}$	7.82	$(1.0\ \pm0.7)\ 10^{-32}$
1.9	$(1.02\pm0.09)\ 10^{-28}$	8.93	$(3\ \ \pm2)\ 10^{-33}$

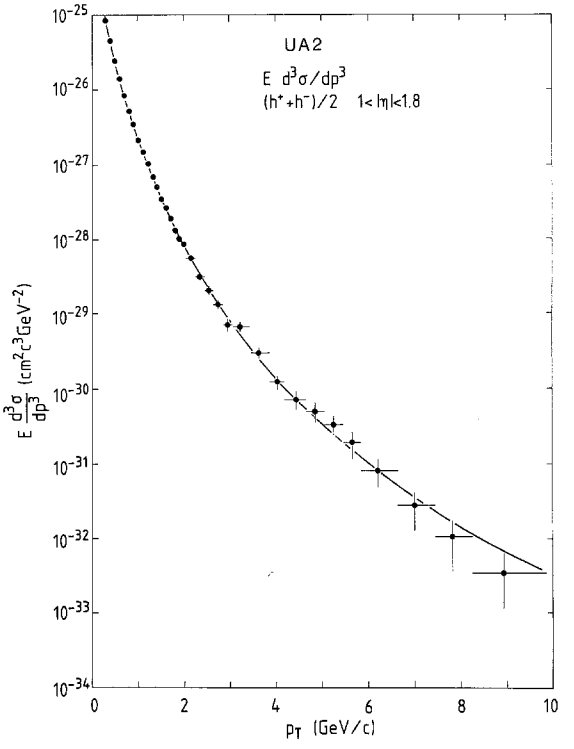

Fig. 5. Invariant cross-section for charged particle production in the F/B detector (the curve is the parametrization described in text)

The overall ratio $R(P_T)$ of positive to negative particle yield is independent of P_T and its average over the entire transverse momentum range is $R=1.02\pm0.01$.

The invariant cross-section values for inclusive charged particle production (charge averaged) are listed in Table 1 and shown in Fig. 5. Figure 6 com-

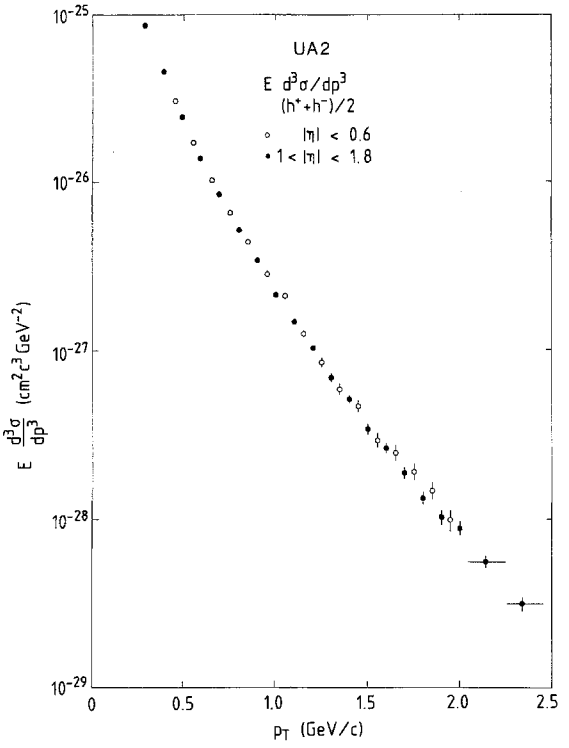

Fig. 6. Invariant cross-section for charged particle production in the F/B detector (full circles) compared to earlier measurement in the wedge detector (open circles, [1])

pares the measurements of this analysis with the charged particle production measured at $\langle\eta\rangle=0$ in the P_T range between 0.45 and 2.5 GeV/c [1]. The latter data have been rescaled in order to account for the value of the inelastic cross-section used in the present paper [8].

The results are compatible with those of the UA1 experiment [9], after a similar rescaling.

4. Neutral Particle Production (π^0 and η)

In the P_T range from 5 to 40 GeV/c, the photons from π^0 decays have a small opening angle and cannot be resolved in the UA2 detector. Therefore π^0 candidates are defined as an energy deposition in the calorimeter compatible with the expected response to photon showers, and having no associated charged track. Most of the high P_T π^0's belong to jets and therefore the probability to find several particles pointing to an energy cluster increases with energy. This phenomenon is referred to, in this paper, as overlap.

There are two types of such overlaps:

a) a π^0 with a charged particle nearby, which leads to a loss of events.

b) a π^0 with one or more additional neutral particles pointing to the same cluster which appear as a single π^0 with a higher P_T.

The cell granularity and the P_T range are different in the F/B and in the wedge regions, and hence the data are analyzed separately in both detectors.

4.1 π^0 Production at $\langle|\eta|\rangle=1.4$

Data are analyzed in the *F/B* calorimeters, over a rapidity range $1.07\leqq|\eta|\leqq1.75$ and for $P_T\geqq6$ GeV/c.

For transverse momenta in the range 6 to 41 GeV/c, the inclusive π^0 cross-section decreases by more than six orders of magnitude. In order to make use of the full luminosity delivered by the machine, three different data samples are considered. Two of them are obtained from a trigger requiring that the transverse energy deposited in any two cells adjacent in θ exceeds a given threshold; this threshold was set at 10 GeV for an integated luminosity of 15.6 nb^{-1} (1982 data), and was set at 15 GeV for an integrated luminosity of 98.3 nb^{-1} (1983 data). The third data sample is obtained from a trigger requiring that the total transverse energy deposited in a sector exceeds 4.5 GeV. It corresponds to an integated luminosity of 0.78 nb^{-1}.

4.1.1. Data Reduction. To minimize the overlap problem, electromagnetic clusters must be defined as small as possible, compatible with a good π^0 detection efficiency.

The F/B calorimeters are located at a distance of 370 cm from the interaction point. The cell size is 27 cm along the θ direction and varies from 33.4 cm to 59 cm along the φ direction, and is therefore much larger than the lateral extension of an electromagnetic shower. The distance between the impact of the two photons in the calorimeter is ~3 cm for a π^0 having $P_T=15$ GeV/c.

For a single cell, the ratio of the two photomultiplier pulse heights measures the average shower position with a precision of 3.5 cm along the φ direction. In the case of two adjacent cells in θ, we require that the shower positions measured in each cell agree within 20 cm for the cells to be merged into a single cluster. This happens in $\sim20\%$ of the cases. In $\sim60\%$ of the cases, at least one of the two γ rays converts and the associated signal in the MTPC tubes provides a localization with a precision of 8 mm in both θ and φ directions. In such cases, two adjacent cells are allowed to merge only if the shower position along θ is less than 5 cm away from the common boundary.

Furthermore, for electromagnetic showers the energy leakage into the second compartment of the calorimeter is expected to be less than 2% of the energy deposited in the first compartment, as measured in test beams. This requirement is imposed on the π^0 candidates. In addition, no track must point to the shower within 20 cm.

The beam halo accompanying the p and $\bar{p}$ bunches can simulate a π^0 in the F/B calorimeters. In this case however, calorimeter signals occur 25 ns earlier with respect to a genuine beam-beam interaction. Such a background has been observed, mainly in sectors located near the median plane of the machine. These events are removed from the data.

4.1.2. Neutron and K_L^0 Contamination. Neutrons and K_L^0 interacting near the entrance to the calorimeter or in the lead-iron converter can simulate π^0's. This contamination can be evaluated statistically by the study of the energy leakage into the second compartment of the calorimeter. Figure 7 shows the distribution of the fraction R of energy leaking into the back compartment. A large peak is observed in the vicinity of $R=0$, as expected for electromagnetic showers, and the presence of a long tail can be interpreted as being due to neutrons and K_L^0. An extrapolation of this tail to $R<2\%$ gives an estimate of this hadronic background $6.3\pm0.8\%$, independent of P_T.

4.1.3. Overlap Corrections. The overlap background is studied using a Monte-Carlo program [10] which gives a reasonable description of the jet production and fragmentation properties observed in this experiment [11, 12]. The Monte-Carlo simulation was checked to agree with the present data on the following points:

a) The neutral cluster transverse energy (E_T) distribution.

b) The relative proportion of identified neutral clusters and of track associated clusters ($\simeq 1$).

c) The distribution of energy in the cells adjacent to the cluster considered.

The simulation is used to estimate the apparent increase of the cross-section due to neutral overlaps $A(E_T)$ and the loss of events due to charged overlaps $B(E_T)$. Since a large fraction of π^0's are part of a jet, the probability of an overlap increases rapidly with E_T. However, charged and neutral overlaps have opposite effects, the overall correction $A(E_T)\times B(E_T)$ remains small (Fig. 8).

4.1.4. Cross-Section. The main contributions to the neutral cluster yield are from π^0, η, and single pho-

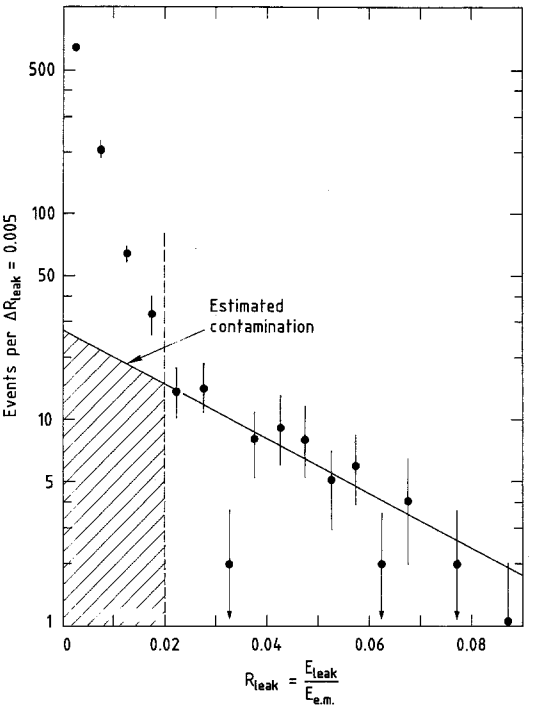

Fig. 7. Distribution of the leakage energy fraction in the F/B calorimeters for neutral clusters

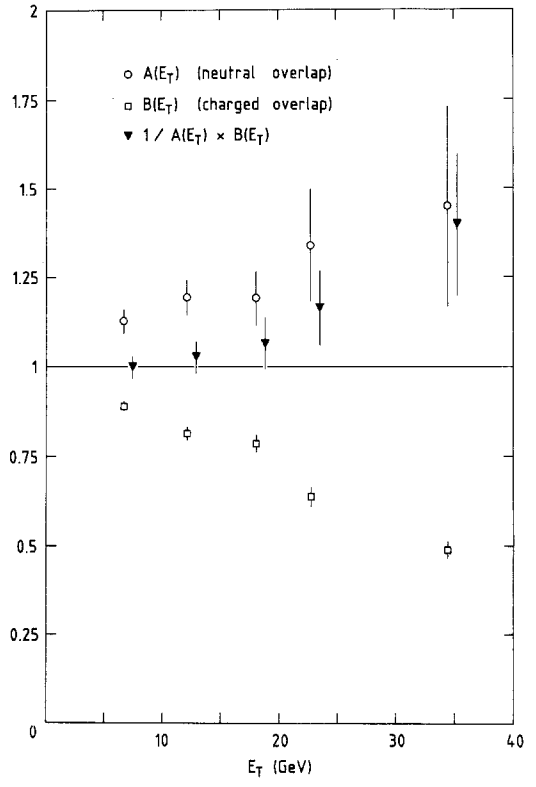

Fig. 8. Overlap correction factors in the F/B detectors. The observed (obs) rate of neutral clusters is related to the true (tr) rate by the following formula:

$(dN/dE_T)_{obs} = (dN/dE_T)_{tr} A(E_T) B(E_T)$

ton production. Since it is impossible to disentangle direct γ's from π^0's, we in fact measure the cross-section for $\pi^0+\gamma$ production. To evaluate the contribution from η-meson decay photons, we assume a $\eta/(\pi^0+\gamma)$ ratio of 0.6 as measured at $\eta=0$ for transverse momenta between 3.3 and 6 GeV/c (see Sect. 4.2.3). This contribution (13% at 15 GeV and 16% at 35 GeV) has been subtracted.

The detector acceptance is estimated by a Monte-Carlo simulation which takes into account all applied cuts. The loss of events due to photon conversion in the beam pipe is also taken into account.

The results are listed in Table 2a.

4.2 π^0 and η Meson Production at $\langle\eta\rangle=0$

Centrally produced π^0 and η mesons are analyzed in the wedge detector for π^0's with P_T exceeding 5 GeV/c, in an effective pseudorapidity interval of $|\eta|\leqq 0.54$. Data were recorded whenever the total energy deposited in the lead-glass wall exceeded a threshold set between 1.8 and 2.8 GeV depending upon the machine luminosity. These data correspond to an integrated luminosity of 16.7 nb^{-1}.

4.2.1. Data Reduction. For each recorded event, the pattern of energy deposition is reduced to a number of clusters by the following algorithm. A cluster is defined as a set of adjacent cells having energies above 100 MeV. A halo contribution from surrounding cells is added to the cluster energy. When the energy distribution within the cluster peaks in two non-adjacent cells, the cluster is split. A cluster is called neutral if no charged track falls within 12 cm from the cluster center.

The reconstruction of a π^0 or an η decaying into two photons is possible when the photons are more than ~ 25 cm apart in the lead-glass wall. A measurement of the π^0 cross-section using this method has been reported in [2], for transverse momenta below 4.5 GeV/c.

We now extend this measurement to $P_T>5$ GeV/c, where the two photons merge into a single cluster. We also measure the production of η mesons decaying into resolved photon pairs ($3.3<P_T<6$ GeV/c).

4.2.2. π^0 Data. Only clusters contained in a three-by-three matrix of lead glass blocks are accepted.

In the P_T range of the present analysis (5 to 15 GeV/c), neutral clusters can be due not only to π^0, but also to single photons, such as direct photons or photons from a η decay, or to neutrons and K_L^0 interacting in the lead-glass. The yield of single photons is expected to be negligible in the present P_T range [13].

The contamination from photons resulting from η decay is evaluated with a Monte-Carlo simulation, assuming that the η/π^0 ratio is 0.6 (see Sect. 4.2.3). It amounts to 6% for transverse momenta below 12.5 GeV/c and increases to 8.7% at 14.5 GeV/c.

The contamination from neutrons and K_L^0 is evaluated by observing that the number of clusters associated with a charged particle amounts to 19% of all clusters independent of the cluster energy. If we assume that the neutral and charged hadrons interact in the same way in the lead-glass, and that the ratio

$$(n+\bar{n}+K_L^0)/(\pi^+ +\pi^- +K^+ +K^- +p+\bar{p})$$

Table 2a. Inclusive π^0 cross-section at $\langle|\eta|\rangle=1.4$ ($p\bar{p}\to\pi^0+$anything at $\sqrt{s}=540$ GeV)

P_T (GeV/c)	$Ed^3\sigma/dP^3$ ($cm^2\,GeV^{-2}c^3$)		P_T (GeV/c)	$Ed^3\sigma/dP^3$ ($cm^2\,GeV^{-2}c^3$)	
6.25	(2.17 ± 0.14)	10^{-32}	18.5	(1.03 ± 0.09)	10^{-35}
6.75	(1.35 ± 0.11)	10^{-32}	19.5	(7.96 ± 0.84)	10^{-36}
7.25	(7.56 ± 0.75)	10^{-33}	20.5	(5.39 ± 0.67)	10^{-36}
7.75	(5.47 ± 0.61)	10^{-33}	21.5	(2.71 ± 0.47)	10^{-36}
8.25	(3.34 ± 0.46)	10^{-33}	23	(2.23 ± 0.29)	10^{-36}
9.0	(1.86 ± 0.23)	10^{-33}	25	(8.26 ± 1.71)	10^{-37}
10	(1.23 ± 0.18)	10^{-33}	27	(6.44 ± 1.46)	10^{-37}
11.25	(5.17 ± 0.86)	10^{-34}	29	(6.80 ± 1.46)	10^{-37}
12.5	(1.84 ± 0.14)	10^{-34}	31.5	(1.61 ± 0.56)	10^{-37}
13.5	(9.81 ± 0.95)	10^{-35}	34.5	(1.38 ± 0.50)	10^{-37}
14.5	(5.80 ± 0.71)	10^{-35}	37.5	(5.76 ± 3.13)	10^{-38}
16	(3.38 ± 0.36)	10^{-35}	41	(3.58 ± 2.06)	10^{-38}
17.5	(1.42 ± 0.12)	10^{-35}			

Table 2b. Inclusive π^0 cross-section at $\langle\eta\rangle=0$. ($p\bar{p}\to\pi^0+$anything at $\sqrt{s}=540$ GeV)

P_T (GeV/c)	$Ed^3\sigma/dP^3$ ($cm^2\,GeV^{-2}c^3$)		P_T (GeV/c)	$Ed^3\sigma/dP^3$ ($cm^2\,GeV^{-2}c^3$)	
5.75	(3.72 ± 0.44)	10^{-32}	10.5	$(8.1\ \pm1.7)$	10^{-34}
6.5	(1.55 ± 0.18)	10^{-32}	11.5	$(4.1\ \pm1.0)$	10^{-34}
7.5	(5.29 ± 0.73)	10^{-33}	12.5	(1.36 ± 0.53)	10^{-34}
8.5	(2.30 ± 0.36)	10^{-33}	13.5	$(7.0\ \pm3.6)$	10^{-35}
9.5	(1.12 ± 0.21)	10^{-33}	14.5	$(6.5\ \pm3.2)$	10^{-35}

Table 2c. Inclusive η meson cross-section at $\langle\eta\rangle=0$. ($p\bar{p}\to\eta+$anything at $\sqrt{s}=540$ GeV)

P_T (GeV/c)	$Ed^3\sigma/dP^3$ ($cm^2\,GeV^{-2}c^3$)	
3.75	(5.65 ± 0.49)	10^{-31}
4.75	(1.26 ± 0.17)	10^{-31}
5.75	(2.40 ± 0.65)	10^{-32}

has the value 0.5 [1], this contamination is $(12\pm7)\%$. The value is consistent with the observed interaction rate of neutral particles as measured in the *WB* hodoscope.

The loss due to the accidental overlap of a neutral cluster with a charged particle is evaluated by extrapolating the distribution of the square of the distance between the neutral cluster centroid and the closest charged track. The loss is $(4\pm2)\%$, and is found to be independent of P_T.

For the contribution of the overlap of two neutral clusters, the same procedure leads to a correction of $(8\pm2)\%$ at 5.5 GeV/c and $(3\pm1)\%$ at 14.5 GeV/c. In this range of P_T, the probability of overlap with another neutral cluster does not depend on P_T. However, the spectrum is less steep at large P_T (14.5 GeV/c) than at low P_T (5.5 GeV/c). For this reason, the accidental addition of a given energy leads to a smaller correction at large P_T than at low P_T.

The detector acceptance is evaluated by a Monte-Carlo simulation. The loss of events due to photon conversion in the beam pipe and in the vertex detector is also taken into account. The measured cross-section is given in Table 2b.

4.2.3. η Meson Data. To search for an η meson signal via its decay into two photons, we study the distribution of the invariant mass of neutral cluster pairs under the following requirements:

a) Each cluster must contain no more than four cells.

b) The asymmetry between the energies of the clusters must be less than 0.4:

$$|(E_1-E_2)/(E_1+E_2)|\leqq 0.4.$$

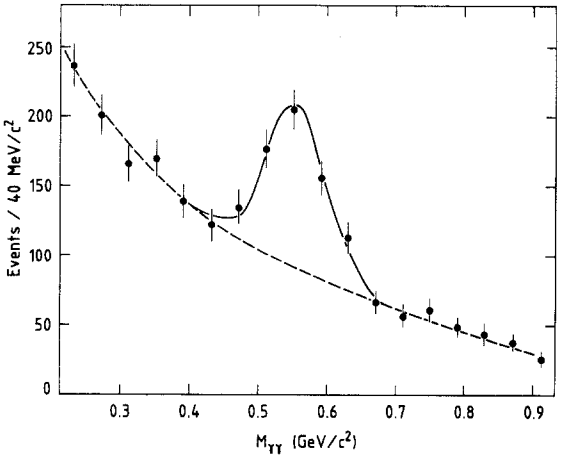

Fig. 9. Invariant mass distribution of photon pairs detected in the wedge, around the η mass. The solid line shows the result of a Monte-Carlo simulation which includes the energy resolution and cell granularity as described in the text, superimposed on a smooth background (dashed line)

The invariant mass distribution, for transverse momenta of the pair above 3.25 GeV/c, displays a clear signal well centered at the η mass, as shown in Fig. 9. The background under the peak is subsequently subtracted in each P_T bin.

The acceptance is evaluated by a Monte-Carlo simulation. In the accessible P_T range (from 3.25 to $\sim$6 GeV/c), it is dominated by the requirement of having both decay photons within the detector aperture, and increases almost linearly with P_T.

Corrections were made to the cross-section for:

a) Loss of events due to overlap with a charged track or a photon: $(+16\pm4)\%$.

b) Photon conversions in the vacuum pipe and the vertex detector: $(+10\pm1)\%$.

The cross-section is given in Table 2c.

5. Discussion of the Results

The measured invariant cross-sections for π^0 and charged particle production were fitted with the empirical formula:

$$Ed^3\sigma/dP^3 = A(P_{T0}/(P_{T0}+P_T))^n$$

The values of the parameters A, n and P_{T0} are listed in Table 3.

Since the shapes of the cross-section for π^0 and charged hadrons ($h=(h^++h^-)/2$) versus P_T are similar in their common P_T range ($1.5<P_T<8.9$ GeV/c), a simultaneous fit of the type above has been performed in this range using the same value of n and P_{T0}.

The ratio $r=A_{\pi0}/A_h$ of the two normalization parameters (A) obtained in these fits measures the relative production rate of π^0 and charged hadrons. It is expected to be smaller than 1, since h includes pions and other charged particles ($K^\pm, p, \bar{p}$).

We obtain $r=2\pi^0/(h^++h^-)=0.68\pm0.13$

The fitted π^0 production cross-section is integrated in the P_T range where the η production is measured, $3.25\leqq P_T\leqq 6$ GeV/c, to evaluate the η/π^0 ratio, $\eta/\pi^0=0.60\pm0.04$ (stat.)±0.15 (syst.), compatible with lower energy ISR measurements [14].

The different results on inclusive cross-sections presented here and in earlier publications [1, 2] are obtained in two pseudorapidity intervals, centered at $\langle\eta\rangle=0$ and $\langle|\eta|\rangle=1.4$. A QCD based calculation (discussed later) shows that the difference increases with P_T (from 20% at 10 GeV/c to 55% at 20 GeV/c). However, in the range of P_T where the measurements at $\langle|\eta|\rangle=1.4$ and at $\langle\eta\rangle=0$ overlap, the difference is expected to be smaller than the errors. The internal consistency of our measurements concerning the agreement between charged particle

Table 3. Fit parameters for $\frac{Ed^3\sigma}{dP^3}=A\left(\frac{P_{T^0}}{P_{T^0}+P_T}\right)^n$, for UA2 data at $\sqrt{s}=540$ GeV

Data	P_T interval (GeV/c)	A ($\mathrm{cm^2\,GeV^{-2}\,c^3}$)	P_{T^0} (GeV/c)	n
$p\bar{p}\to\pi^0+x$	1.5–41	$(1.66\pm0.22)\ 10^{-21}$	0.207 ± 0.004	7.26 ± 0.03
$p\bar{p}\to h+x$	0.3–8.9	$(7.73\pm0.28)\ 10^{-25}$	0.865 ± 0.009	7.66 ± 0.06

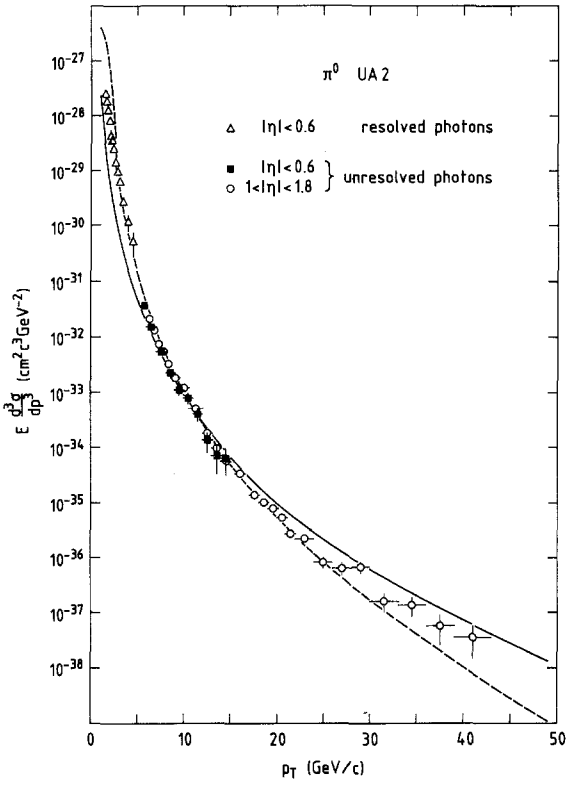

Fig. 10. Inclusive π^0 production cross-section. The curves correspond to a QCD based calculation with different choices of the parameters: a) structure function from [15], $Q^2=P_T^2$, $\Lambda=0.25$ GeV (solid curve). b) structure function from [16], $Q^2=P_T^2$, $\Lambda=0.5$ GeV (dashed curve).
The predicted cross-section also depends on the fragmentation function. The function used here is from [17] and includes scaling violations. If scaling violations are not included the predicted cross-section increases. This increase is less than a factor 1.5 for $P_T<12$ GeV/c, and reaches a factor 2 at $P_T=30$ GeV/c

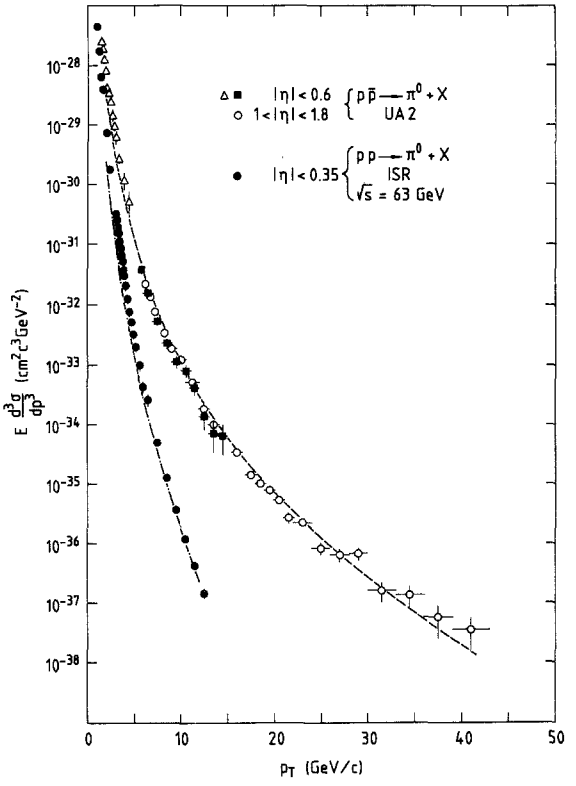

Fig. 11. Comparison of the invariant cross-sections for inclusive π^0 production as measured in UA2 at $\sqrt{s}=540$ GeV, and at the ISR [18] at $\sqrt{s}=63$ GeV. The (dashed and dot-dashed respectively) curves are the corresponding predictions of the QCD based calculation, using the structure and fragmentation functions from [17], $Q^2=P_T^2$, $\Lambda=0.31$ GeV

(respectively π^0) production at $\langle\eta\rangle=0$ and at $\langle|\eta|\rangle=1.4$ is shown in Fig. 6 (respectively Fig. 10).

Figure 10 compares the measured π^0 cross-section with predictions of a QCD calculation describing the hard parton scattering and their fragmentation into hadrons. It proceeds as follows:

– The longitudinal momenta of initial partons inside the incoming p and $\bar{p}$ are taken according to the structure functions measured in deep inelastic scattering experiments [15–17].

– The initial partons scatter according to lowest-order QCD scattering cross-sections.

– The final partons fragment into hadrons according to the fragmentation functions from [17].

Structure and fragmentation functions are evolved with Q^2.

The agreement between the experimental and calculated cross-sections is good. The uncertainty in the calculated value due to the choice of input parameters (structure and fragmentation functions, value of the QCD scale parameter Λ) can reach a factor of about 6 at 40 GeV/c, small in comparison with the ten orders of magnitude variation of the cross-section over the whole P_T range.

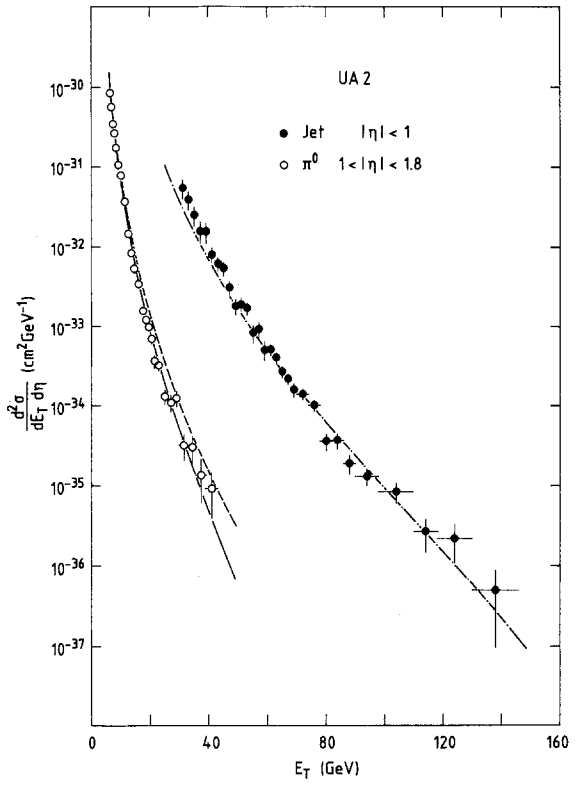

Fig. 12. Comparison of the cross-sections for inclusive jet and π^0 productions. The curves are the predicted jet cross-section at $\eta=0$ (— · —) and π^0 cross-section at $\eta=0$ (— — —) and at $\eta=1.4$ (——). The calculation uses the structure and fragmentation functions from [17], $Q^2=P_T^2$, $\Lambda=0.31$ GeV

The ratio of π^0 and jet inclusive productions is also well predicted: Fig. 12 shows the inclusive jet production cross-section $(d^2\sigma/dP_T d\eta)$ at $\eta=0$, measured in the UA2 experiment [11] together with the measured π^0 cross-section at $\eta=1.4$, and the corresponding predictions.

A comparison with the π^0 cross-section measured at lower energies [18] is shown in Fig. 11, together with the corresponding predictions. The calculation describes well the large increase of the observed cross-sections from ISR to collider energy.

Thus the hadronic interactions are well described by the parton model derived from lowest order QCD in the large Q^2 limit.

Conclusions

Results of the UA2 experiment on inclusive particle production at the CERN $Sp\bar{p}S$ collider have been presented. Measurements of the following invariant cross-sections are presented:

a) charged particle production in the range:

$0.25\ \text{GeV/c} \leqq P_T \leqq 10\ \text{GeV/c}$ at $\langle|\eta|\rangle = 1.4$,

b) π^0 production in the range:

$6\ \text{GeV/c} \leqq P_T \leqq 40\ \text{GeV/c}$ at $\langle|\eta|\rangle = 1.4$,

c) π^0 production in the range:

$5.5\ \text{GeV/c} \leqq P_T \leqq 15\ \text{GeV/c}$ at $\langle\eta\rangle = 0$.

The ratio of η meson to π^0 yields is measured to be

$0.60 \pm 0.04\ (\text{stat.}) \pm 0.15\ (\text{syst.})$

A QCD based calculation satisfactorily describes the π^0 production spectrum over the P_T range 1.5 GeV/c to 40 GeV/c, that is over a range of 10 orders of magnitude in the measured cross-section.

Acknowledgements. This experiment would have been impossible without the collective effort of the staffs and coordinators of all accelerators involved in the operation of the CERN $\bar{p}p$ Collider, whom we gratefully acknowledge.

We deeply thank the technical staffs of the institutes collaborating in UA2 for their important contributions.

We are grateful to the UA4 Collaboration for providing the signals from their small-angle scintillator arrays.

Financial supports from the Schweizerischer Nationalfonds zur Förderung der Wissenschaftlichen Forschung to the Bern group, from the Danish Natural Science Research Council to the Niels Bohr Institute group, from the Institut National de Physique Nucleaire et de Physique des Particules to the Orsay group, from the Istituto Nazionale di Fisica Nucleare to the Pavia group and from the Institut de Recherche Fondamentale (CEA) to the Saclay group are acknowledged.

References

1. M. Banner et al.: Phys. Lett. **122B**, 322 (1983)
2. M. Banner et al.: Phys. Lett. **115B**, 59 (1982)
3. B. Mansoulié: The UA2 apparatus at the CERN $p\bar{p}$ Collider, Proceedings 3rd Moriond workshop on $p\bar{p}$ physics, p. 609. editions Frontieres, 1983
4. M. Dialinas et al.: The vertex detector of the UA2 experiment. LAL-RT/83-14, ORSAY, 1983
5. C. Conta et al.: Nucl. Instrum. Methods **224**, 65 (1984)
6. K. Borer et al.: Multitube proportional chambers for the localization of electromagnetic chambers in the UA2 detector, CERN-EP/83-177, submitted to Nucl. Instrum. Methods
7. A. Beer et al.: Nucl. Instr. Meth. **224**, 360 (1984)
8. R. Battiston et al.: Phys. Lett. **117B**, 126 (1982)
9. G. Arnison et al.: Phys. Lett. **118B**, 167 (1982)
10. ISAJET program, F. Paige, S. Protopopescu: BNL Report 31987 (1981)
11. P. Bagnaia et al.: Phys. Lett. **138B**, 430 (1984)
12. P. Bagnaia et al.: Phys. Lett. **144B**, 283, 291 (1984)
13. A.P. Contogouris, M. Sanielevici: CERN-TH/3656; R. Horgan, M. Jacob: Nucl. Phys. **B179**, 441 (1981)
14. F.W. Busser et al.: Phys. Lett. **55B**, 232 (1975); K. Eggert et al.: Nucl. Phys. **B58**, 49 (1975); C. Kourkoumelis et al.: Phys. Lett. **84B**, 277 (1979)
15. H. Abramovicz et al.: Z. Phys. C – Particles and Fields 12, 289 (1982); F. Eisele: private communication
16. J.F. Owens, E. Reya: Phys. Rev. **D17**, 3003 (1978)
17. R. Baier, J. Engels, B. Petersson: Z. Phys. C – Particles and Fields **2**, 265 (1979)
18. C. Kourkoumelis et al.: Z. Phys. C – Particles and Fields **5**, 95 (1980)